PCCP

PAPER

View Article Online
View Journal | View Issue

Cite this: *Phys. Chem. Chem. Phys.*, 2024, **26**, 5548

MoO_3 nanowire growth on VO_2/WO_3 for thermochromic applications†

Amina Houimi,[ab] Mohamed A. Basyooni-M. Kabatas, *[acd] Mucahit Yilmaz [e] and Yasin Ramazan Eker[af]

Received 6th December 2023,
Accepted 17th January 2024

DOI: 10.1039/d3cp05942a

rsc.li/pccp

This study explores the structural, electronic, and optical properties of sandwich-structured thin films composed of WO_3, $MoWO_3$, and MoO_3 as window layers on VO_2/WO_3 *via* a physical vapor deposition method. Morphological analysis demonstrates the evolution of distinct nanowires, offering insights into the lattice strain of the VO_2 layer toward high-performance thermochromatic devices. Temperature-dependent sheet resistivity is investigated, showcasing significant improvements in conductivity for samples with MoO_3 as a window layer. The electrical and optical properties of the $MoO_3/VO_2/WO_3$ device showed a phase transition temperature (T_c) of 36.8 °C, a transmittance luminous (T_{lum}) of 54.57%, and a solar modulation ability (ΔT_{sol}) of 12.43. This comprehensive analysis contributes to understanding the growth of nanowires on multi-layered thin films, offering valuable insights into potential applications in bright windows.

I. Introduction

Building services use more energy than the transportation and industrial sectors, accounting for over half of all energy consumption. Most energy is used to run different heating, ventilation, and air conditioning (HVAC) systems.[1,2] The development of efficient energy conversion technologies is of utmost importance in the modern era, and thermochromic materials are a promising avenue in this regard.[3] In particular, the thermochromic properties of VO_2 have received significant attention in recent years due to their potential for use in various applications, such as temperature sensors, energy harvesting, and cooling devices. The ability of VO_2 to undergo a reversible phase transition from an insulating to a metallic state with a change in temperature makes it an ideal candidate for thermochromic applications.[4,5] However, in the real-world implementation of VO_2-based thermochromic bright windows, issues with high T_c, balancing the T_{lum}, and ΔT_{sol} still persist. Since high T_c limits the practical usage of monolayer VO_2 films, T_c is reduced by a variety of techniques, including strain engineering,[6] element doping,[7] and multilayer construction.[8–10] Monoclinic VO_2 has been synthesized using various fabrication methods, each of which has proven successful in producing high-performance materials, such as chemical vapor deposition (CVD),[11] pulsed laser deposition (PLD),[12] molecular beam epitaxy (MBE),[13] and liquid phase synthesis (LPS).[14] These various methods have each demonstrated remarkable performance characteristics.

The thermochromic properties of VO_2 can be further enhanced through sandwich structures, consisting of layers of different materials stacked on top of each other. In addition to significantly improving the VO_2 crystal's quality, window layers with lattice characteristics equivalent to VO_2 can act as a barrier against particle diffusion between the intermediate layer and the substrate and act as an antireflecting layer (ARL).[15,16] The T_c and thermal hysteresis width (ΔH) of the VO_2 layer can be altered by the internal tension brought on by a lattice mismatch.[17,18] In general, carefully considering the materials employed is necessary to attain the appropriate optical characteristics in constructing sandwich structures. The materials selected will be determined by the particular application and the required performance standards.[19] In a particular way, the envisioned advantage of nanowire structures for smart windows lies in the potential to fine-tune the metal–insulator transition at lower temperatures, facilitating better control over the window's transparency in response to external stimuli. Nanowires, with their higher aspect ratio and altered optical properties, can influence the transmittance luminosity of smart

[a] *Science and Technology Research and Application Center (BITAM), Necmettin Erbakan University, Konya 42090, Turkey. E-mail: m.a.basyooni@gmail.com*
[b] *UNAM, Institute of Materials Science and Nanotechnology, Bilkent University, Ankara 068000, Turkey*
[c] *Dynamics of Micro and Nano Systems Group, Department of Precision and Microsystems Engineering, Delft University of Technology, Mekelweg 2, 2628 CD Delft, The Netherlands. E-mail: m.kabatas@tudelft.nl*
[d] *Solar Research Laboratory, Solar and Space Research Department, National Research Institute of Astronomy and Geophysics, 11421 Cairo, Egypt*
[e] *Department of Fundamental Science, Necmettin Erbakan University, Konya, Turkey*
[f] *Department of Basic Sciences, Faculty of Engineering, Necmettin Erbakan University, Konya 42090, Turkey*

† Electronic supplementary information (ESI) available. See DOI: https://doi.org/10.1039/d3cp05942a

windows. Their unique geometry and changed interaction with light might enhance light scattering or absorption properties compared to nanoparticles such as the recently reported, plasmonic Au nanowires,[20] silver nanowires,[21,22] WO_3 nanowires,[23] Sb_2Se_3 ultrathin nanowires,[24] and VO_2 nanowires.[25]

This article investigates the effect of Mo, W, and Mo-W oxide window layers in the ARL coating on the thermochromic properties of VO_2/WO_3 sandwich structures on the FTO glass substrate. Our study focuses on understanding the impact of Mo concentration on the shape of the nanowires, the electrical and optical properties of sandwich structures, and how these properties affect the overall thermochromic performance of the VO_2. The surface morphology plays a significant role in thermochromic applications, particularly in enhancing parameters like transmittance luminous (T_{lum}) and solar modulation ability (ΔT_{sol}).

II. Materials and methods

1. Deposition of sandwich structures

The thin film multi-layers comprising vanadium (V), molybdenum (Mo), and tungsten (W) were prepared using metallic targets of three inches with a purity of 99.9%. The deposition process involved reactive radio frequency (RF) and direct current (DC) magnetron sputtering, utilizing a combination of argon and oxygen gases, as detailed in Table 1. Before sputtering, the chamber underwent a vacuum pump down to a pressure of 7×10^{-7} Torr. Cleaned FTO (6 Ω square^{-1}) substrates were utilized for depositing the thin films. These FTO glass substrates were cleaned under ultrasonic conditions with acetone and isopropyl alcohol for 15 min, followed by rinsing with deionized water and high-purity nitrogen gas. All samples were heated to the desired temperature in the sputtering chamber and left for 30 minutes to stabilize the substrate temperature. A working pressure of 5.1×10^{-3} Torr was maintained throughout the processes. The thicknesses of the V–O, W–O, and Mo–O films were controlled by adjusting the deposition time. By keeping constant film deposition times, the film thicknesses of V–O, W–O, Mo–O, and Mo–W–O films were consistent across all samples. The deposition parameters are illustrated in Table 1. The deposition parameters control the window layer's nanowire growth through the materials' deposition rate.

While $Mo_{0.2}W_{0.8}O_3$ was a composite film combining Mo and W, the film was created under specific conditions, with an oxygen environment of 12.1 sccm and an argon flow of 50 sccm, and the power applied to the Mo and W targets during the deposition process was 27 W and 110 W, respectively. The entire deposition process lasted 16.7 minutes for both Mo and W targets. The primary objective of this layer was to incorporate a small quantity of Mo atoms into the WO_3 film to produce a high-quality layer with anti-refractive and anti-oxidative properties. Our previous research[26–28] has indicated that this layer exhibits exceptional transmission characteristics and favorable electrical performance. It is worth noting that the optimization of the Mo content within the WO_3 film has been thoroughly explored in previous studies.[28] Moreover, following the sputtering process, VO_2 was subjected to an *in situ* treatment at a temperature of 400 °C for 2 hours, with an argon flow rate of 50 sccm.

For simplicity, V, W–V–W, MoW–V–W, and Mo–V–W are used which represented the VO_2, $WO_3/VO_2/WO_3$, $Mo_{0.2}W_{0.8}O_3/VO_2/WO_3$, and $MoO_3/VO_2/WO_3$ samples.

Table 1 The deposition parameters of the deposited multilayer films

Parameters	V–O	W–O	Mo–O	Mo–W–O
Power (W)	DC_V/190	RF_W/137	RF_M/137	RF_{M-W}/137
Ar (sccm)	41	37.1	37.1	37.1
O_2 (sccm)	2.2	12.1	12.1	12.1
Time (min)	7.5	7.5	16.7	16.7
Thickness (nm)	50	100	100	120

2. Characterization techniques

The optical transmission (T) was evaluated using a UV-Vis-NIR spectrophotometer attached to a heating stage, specifically the UV-3600i Plus model by Shimadzu. The surface morphology was analyzed using a field emission scanning electron microscope (FESEM), specifically the ZEISS GeminiSEM 500. Raman vibrational modes were captured using a Renishaw inVia confocal Raman microscope with a 532 nm laser beam. X-ray photoelectron spectroscopy (XPS) measurements were performed using a Thermo Scientific K-alpha XPS system, employing an Al Kα source and a spot size of 400 μm. A source meter system measured the electrical I–V phase transition under temperature changes, including a connected heating stage. An *in situ* Quartz crystal monitor within the sputtering system collected the thickness measurements. Additionally, a Filmetrics F20 Thin Film Analyzer is used to corroborate the sample thickness, showcasing a minimal deviation of around 1 nm.

III. Results and discussion

1. Structural properties (Raman spectroscopy)

In Fig. S2(b) (ESI†), in the additional information section, the XRD pattern of the deposited VO_2 thin film is presented, indicating a monoclinic phase with a JCPDS card number [#96-153-0871] and a space group of C12/m1(12). Various diffraction peaks appear at 2θ = 15.45°, 20.49°, 31.28°, 47.69°, and 62.32°. The unit cell parameters are a = 12.03000 Å, b = 3.69300 Å, and c = 6.42000 Å, with an angle of β = 106.100°. Fig. S2(c) (ESI†) in the additional information section shows the Raman spectra of VO_2 thin films. The most crucial peaks within the VO_2 layer are related to lattice motion involving V–V bonds (at 132 and 229 cm^{-1}), along with the vibrational modes of V–O bonds in the VO_2 monoclinic insulating phase (at 500 and 828 cm^{-1}).[29–31]

It is also more interesting to present the Raman spectra of MoO_3, WO_3, and $Mo_{0.2}W_{0.8}O_3$ thin films, as represented in Fig. S3 (ESI†) in the additional information section. In the

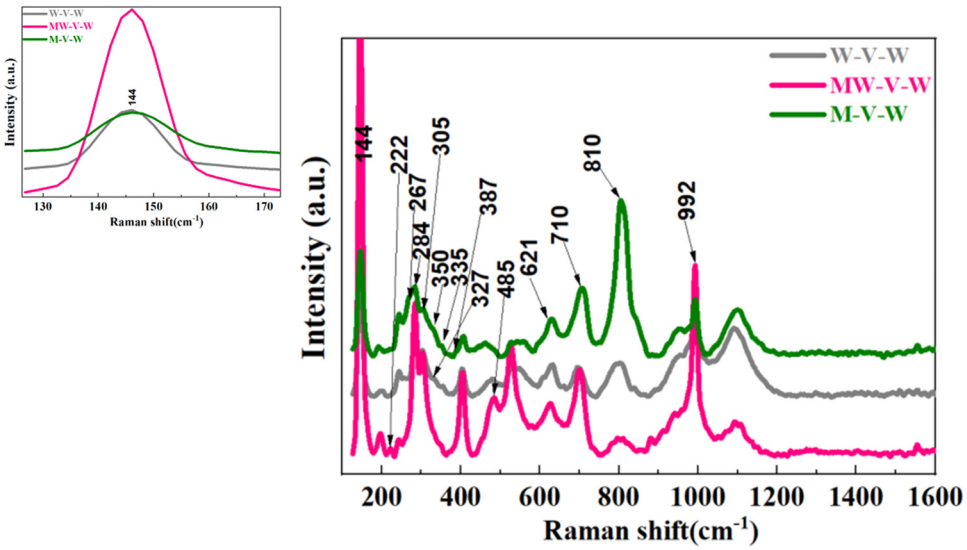

Fig. 1 Raman spectra of W–V–W, MoW–V–W, and Mo–V–W samples. The inset shows the main VO_2 peak at 144 cm^{-1}.

MoO_3 thin film, the prominent peaks at 820, 860, and 994 cm^{-1} correspond to the α-MoO_3 crystal phase and M–O stretching modes.[32–34] Weaker peaks at 190, 283, 336, and 352 cm^{-1} are linked to Mo–O bending mode,[35,36] while the 658 cm^{-1} peak relates to triply coordinated oxygen $Mo_{3\text{-}O}$ stretching.[37] In the WO_3 layer, the monoclinic phase is characterized by peaks at 270 and 326 cm^{-1}.[38] The WO_3 structure is confirmed through the lattice mode peak at 132 cm^{-1}[39] and stretching mode peaks of W–O–W bonding at 711 and 810 cm^{-1}.[38] For $Mo_{0.2}W_{0.8}O_3$ thin films, Raman peaks are weak, whereas distinguishable prominent peaks for WO_3 imply significant structural disruption caused by the introduction of Mo.

Nevertheless, examining the multilayer sandwich structures of the prepared samples can provide additional insights into the strain effects of VO_2, as illustrated in Fig. 1. Within the VO_2 layer, specific peaks play a crucial role in characterizing the lattice motion involving V–V bonds (132, 144 387, 305 and 222 cm^{-1}), as well as the vibrational mode of V–O bonds in the VO_2 monoclinic insulating phase (500 and 828 cm^{-1}).[29–31,40,41] In the case of the top MoO_3 thin layer, the most robust peaks observed at 820, 860, and 992 cm^{-1} correspond to the α-MoO_3 crystal phase and the M–O stretching modes.[32–34] Additionally, weaker peaks are detected at 191, 284, 335, and 350 cm^{-1}, which are attributed to the bending mode of Mo–O,[35,36] while the peak at 658 cm^{-1} is associated with the triply coordinated oxygen Mo_3–O stretching.[37] Moving on to the WO_3 layer, the monoclinic phase is identified by peaks at 267 and 327 cm^{-1}.[38] The WO_3 lattice mode is confirmed by the peak observed at 133 cm^{-1},[42] and the stretching mode peaks of W-O-W bonding are scanned at 710 and 810 cm^{-1}.[43] Finally, the Raman peaks of $Mo_{0.2}W_{0.8}O_3$ thin films exhibit moderate intensity.

2. Surface morphology of the top window-layer

It is known that VO_2 is one of the attractive, strongly correlated oxides that involve high lattice strain effects that can easily control the deposition of various materials on its surface. Different studies show that reactive DC magnetron sputtering is used to deposit nanowires and nanorods with a high aspect ratio.[44] The growth of different morphologies of VO_2 has been controlled in the sputtering system, as reported before.[45] Our previous research[28] delved into the growth patterns of various metal oxides at 400 °C. Fig. S1(a) and (b) (ESI†) in the additional information section show the surface structures of VO_2 and MoO_3 thin films. By employing high vacuum conditions during deposition, coupled with an optimal sputtering temperature of 40 °C, we achieved the ideal setting for generating nanostructures and uniformly distributed thin films. Notably, nanowires manifest in VO_2, while MoO_3 exhibits growth in the form of nanosheets. However, depositing the sandwich structure affects the surface growth of the VO_2 layer due to its lattice strain, which can influence the growth of MoO_3 on its surface.

The top FE-SEM images of W–V–W, MoW–V–W, and Mo–V–W sandwich samples unveil a fascinating evolution of nanowire-based structures, shedding light on the intricate nature of these composite materials. In Fig. 2(a) and (b), the W–V–W sample exhibits an initial morphology characterized by a dense and compact structure, with large grains (approximately 139 nm in size) uniformly distributed. However, in Fig. 2(c) and (d), with an increased concentration of Mo in the top layer of the MoW–V–W sample, the presence of delicate nanowires becomes evident, signifying the early stages of surface morphology transformation. Observations indicate the presence of nanostructured wires, with dimensions of roughly 60 nm in length and 20 nm in diameter, which appear to develop atop the grains. This formation results in clearly demarcated regions separated by grain boundaries.

As the process continues, further increasing the Mo atom concentration until reaching MoO_3 on the top surface, a profound transformation is observed, resulting in a well-defined and visible nanostructured surface. Fig. 2(e) and (f) depicts the Mo–V–W sample, where short nanowires are uniformly distributed across the entire surface. Notably, the

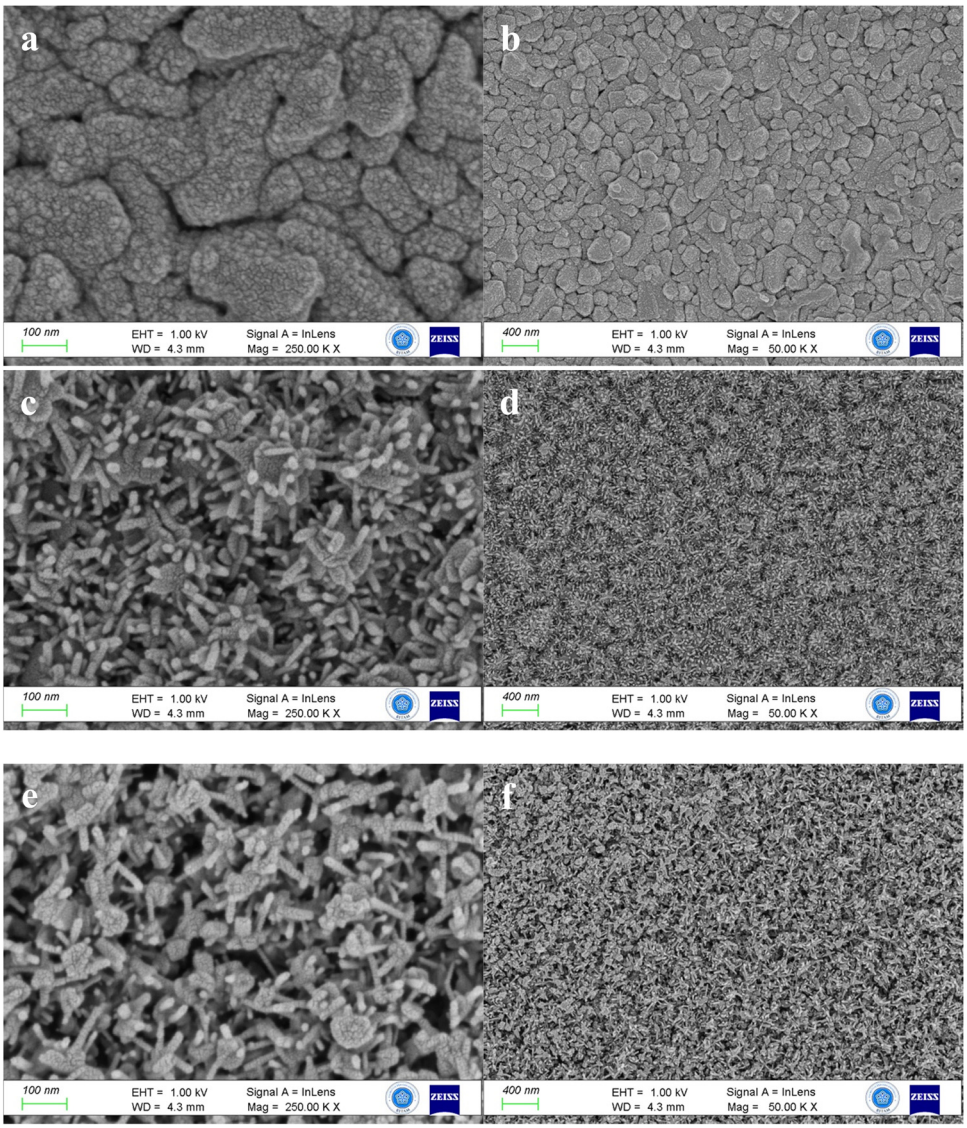

Fig. 2 FE-SEM images of (a) and (b) W–V–W, (c) and (d) MoW–V–W, and (e) and (f) Mo–V–W samples. (a), (c), and (e) show a high resolution of 250 KX, while (b), (d), and (f) represent 50 KX resolutions.

nanoparticles' size remains unchanged compared to the MoW–V–W sample. These short nanowires, characterized by their slender and tapered structures, significantly contribute to the overall surface texture, providing a light-harvesting surface that holds great promise for applications in intelligent windows.

3. XPS

To seek the origin of different thermochromic properties of samples upon varying the top layer of the sandwich structure, the XPS analysis is carried out on both the Mo–V–W and W–V–W samples to examine the composition and valence states of the prepared films. The corresponding results are displayed in Fig. 3 and 4. In Fig. 3(a), the analysis of Mo–V–W and the XPS spectra revealed the presence of the V2p, O1s (Fig. 3(b)), and Mo3d (Fig. 3(c)) photoelectron spectra. The peaks were deconvoluted using a Gaussian function to ascertain the films' chemical state and stoichiometry. Due to spin–orbit splitting, the $V2p_{3/2}$ spectra display characteristic two-peak patterns at 517.1 eV and 517.9 eV, corresponding to the oxidation states of V^{4+} and V^{5+}, respectively. For O1s, the core peak was split into two peaks corresponding to an oxygen ion "O^{2-}" at 530 eV and oxygen vacancies "V_O^{2+}" at 533.12 eV. High-resolution XPS in Fig. 3(c) showed the enlarged spectra of Mo3d between 227 eV and 240 eV binding energies, which exhibited dual peaks, with $Mo3d_{5/2}$ and $Mo3d_{3/2}$ peaks. These peaks correspond to molybdenum in Mo^{6+} oxidation states. The binding energy difference of $Mo3d_{5/2}$ and $Mo3d_{3/2}$ is 3.12 eV, which fits well with the reported values.[46,47]

The XPS analysis of the W–V–W sample is presented in Fig. 4. The survey spectrum in Fig. 4(a) shows the existence of O, W, and V. Deconvolution of $V2p_{3/2}$ also reveals two peaks at 516.41 eV and 517.11 eV, for V^{4+} and V^{5+}, oxidation states,

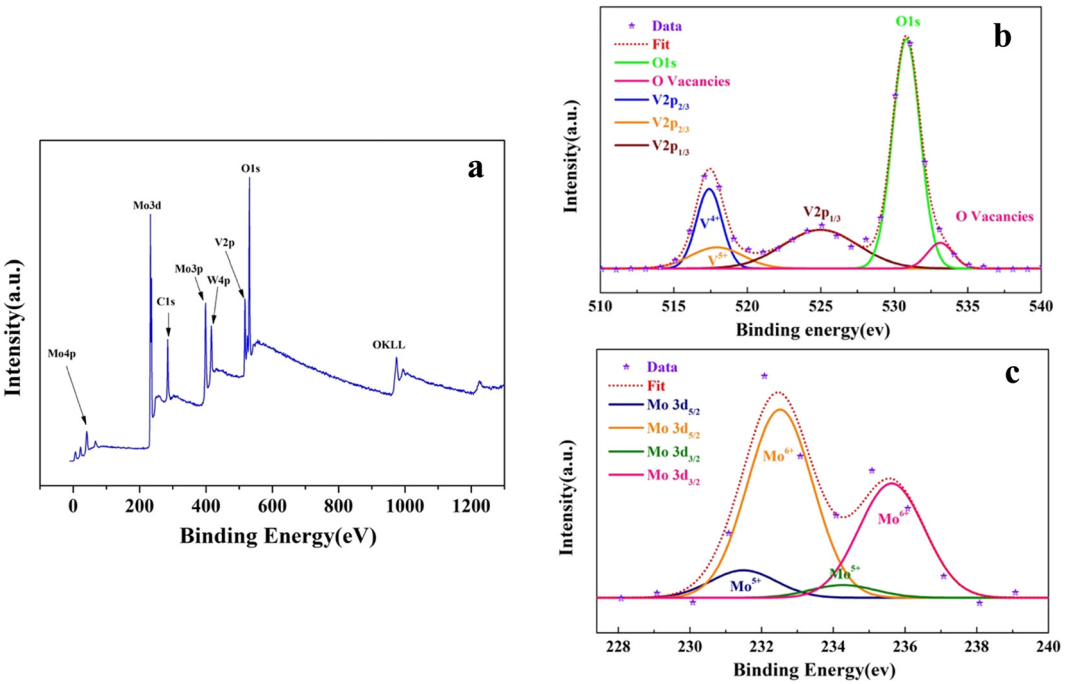

Fig. 3 (a) XPS survey spectrum of the M–V–W sample. (b) Enlarged spectra of V $2p_{3/2}$, V $2p_{1/2}$, and O 1s and (c) Mo 3d peaks.

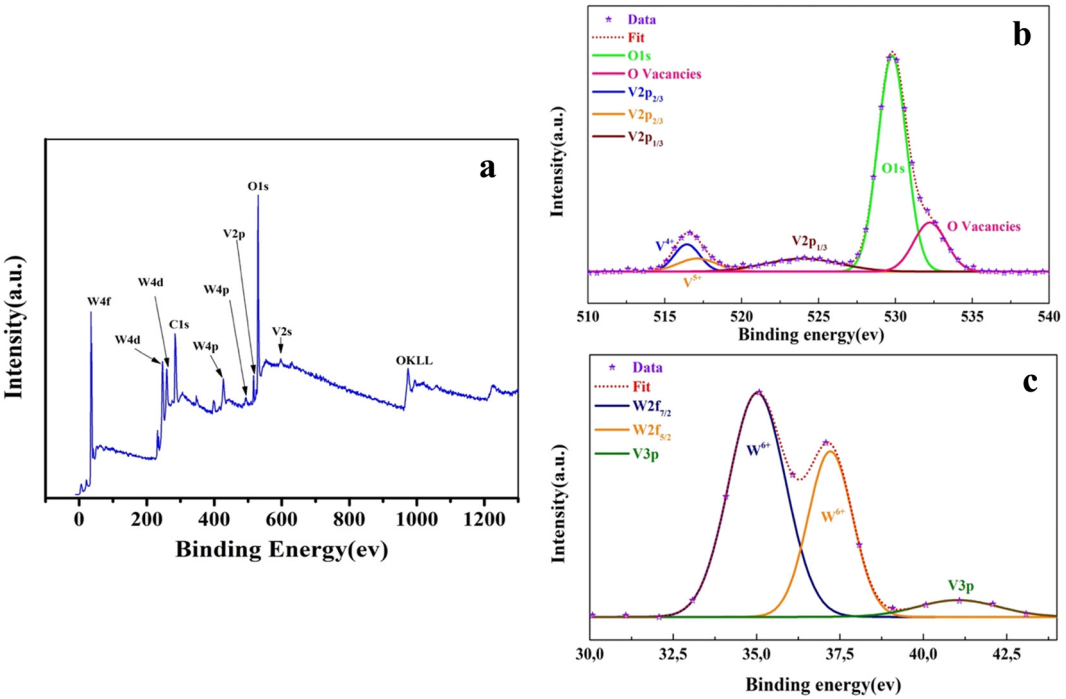

Fig. 4 (a) XPS survey spectrum of the W–V–W sample. (b) Enlarged spectra of V $2p_{3/2}$, V $2p_{1/2}$, and O 1s and (c) W 2f and V 3p peaks.

respectively. The high resolution of the O1s core peak shows an oxygen ion peak of "O^{2-}" at 529.78 eV and oxygen vacancies "V_O^{2+}" at 532.24 eV (Fig. 4(b)).[48] In addition, from the deconvolution of the W4f core peak in Fig. 4(c), W is present as W^{6+} with $W4f_{7/2}$ and $W2f_{5/2}$ at 35.02 eV and 37.21 eV binding energies, respectively. These binding energies were consistent with previously published values of the W^{6+} oxidation state WO_3.[38,42]

The integrated surface ratio of V^{4+}/V^{5+} in Mo–V–W is 1.87, indicating a higher proportion of V^{4+} valence than the W–V–W

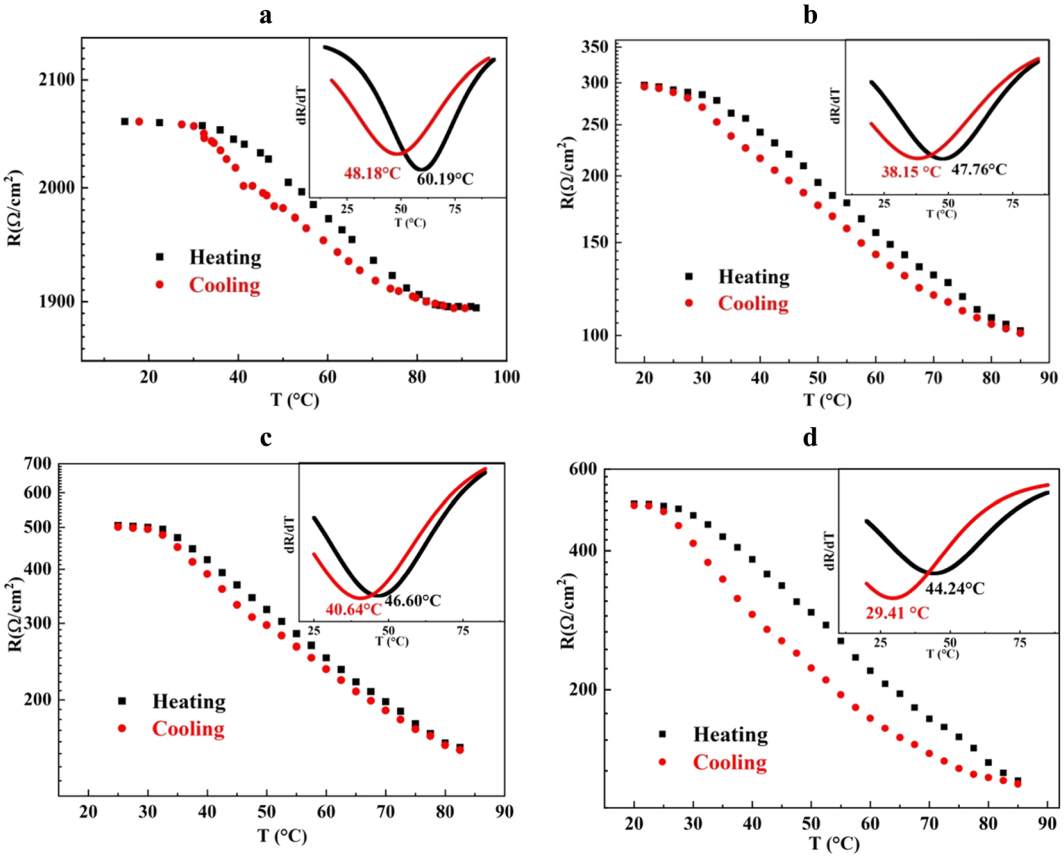

Fig. 5 Temperature-dependent sheet resistivity of (a) V, (b) W–V–W, (c) MoW–V–W, and (d) Mo–V–W samples. T_c calculated from d(log R)/dT ~ T with Gauss fitting plots in insets.

sample, which presents a lower V^{4+}/V^{5+} ratio of 1.37. It is generally thought that W^{6+} and Mo^{6+} as solutes penetrate the crystal lattice of VO_2 and substitute the V^{4+} ion, creating donor-like defects (both W^{6+} and Mo^{6+} ions with valences higher than V^{4+} ions). The lower V^{4+}/V^{5+} ratio in the W–V–W sample relative to the Mo–V–W sample is attributed to the possibility of over-doping VO_2 thin films by W atoms migrating from both upper and lower layers.[47] However, in the Mo–V–W sample, the co-doping of W^{6+} and Mo^{6+} ions contribute separately to the increasing V^{4+}/V^{5+} ratio.[19,49,50]

4. Electrical properties

Fig. 5 illustrates the temperature-dependent sheet resistivity of V, W–V–W, MoW–V–W, and Mo–V–W samples. The graph showcases the variation in sheet resistivity with changing temperatures. Initially, all samples exhibit thermochromic properties with a relatively high sheet resistivity in KΩ order (Table 2). As the temperature increases, a significant decrease in sheet resistivity of up to four orders of magnitude is observed for the samples with MoO_3 as a window layer. This remarkable change indicates a notable improvement in the electrical conductivity properties of the sandwich samples compared to the reference sample V.

The amplitude of transition (ΔR), representing the resistance change from room temperature above 85 °C, and the hysteresis widths (ΔH), calculated as the difference between T_c values measured during heating and cooling cycles are also discussed. The T_c value of the W–V–W sample with a WO_3 window layer is 43 °C, while for the MoW–V–W sample with a $Mo_{0.2}W_{0.8}O_3$ window layer, it is 43.6 °C. However, Mo–V–W samples presented the lowest recorded T_c behavior of 36.8 °C. Those values of the three samples are lower than the observed transition temperature of VO_2 of the order 54 °C.

Table 2 T_c, ΔR and ΔH of V, W–V–W, MoW–V–W, and Mo–V–W samples

Samples	T_c (°C)	ΔR (Ω cm^{-1})	ΔH (°C)
V	54	1.7×10^2	12
W–V–W	43	1.95×10^2	9.6
MoW–V–W	43.6	3.5×10^2	6
Mo–V–W	36.8	3.78×10^2	14.8

Furthermore, the ΔR and ΔH values change according to the window layer used in W–V–W, MoW–V–W, and Mo–V–W samples. Comparatively, the W–V–W sample deposited with a WO_3 window layer exhibits a lower ΔR value of 1.95×10^2 Ω cm^{-2}, while MoW–V–W with the $Mo_{0.2}W_{0.8}O_3$ window layer presented a narrower ΔH of 6 °C with a high ΔR of 3.5×10^2 Ω cm^{-2}, indicating superior electrical behavior compared to the V sample with the smallest ΔR (1.7×10^2 Ω cm^{-2}) and a ΔH value of 12 °C. Mo–V–W presented a higher ΔR of

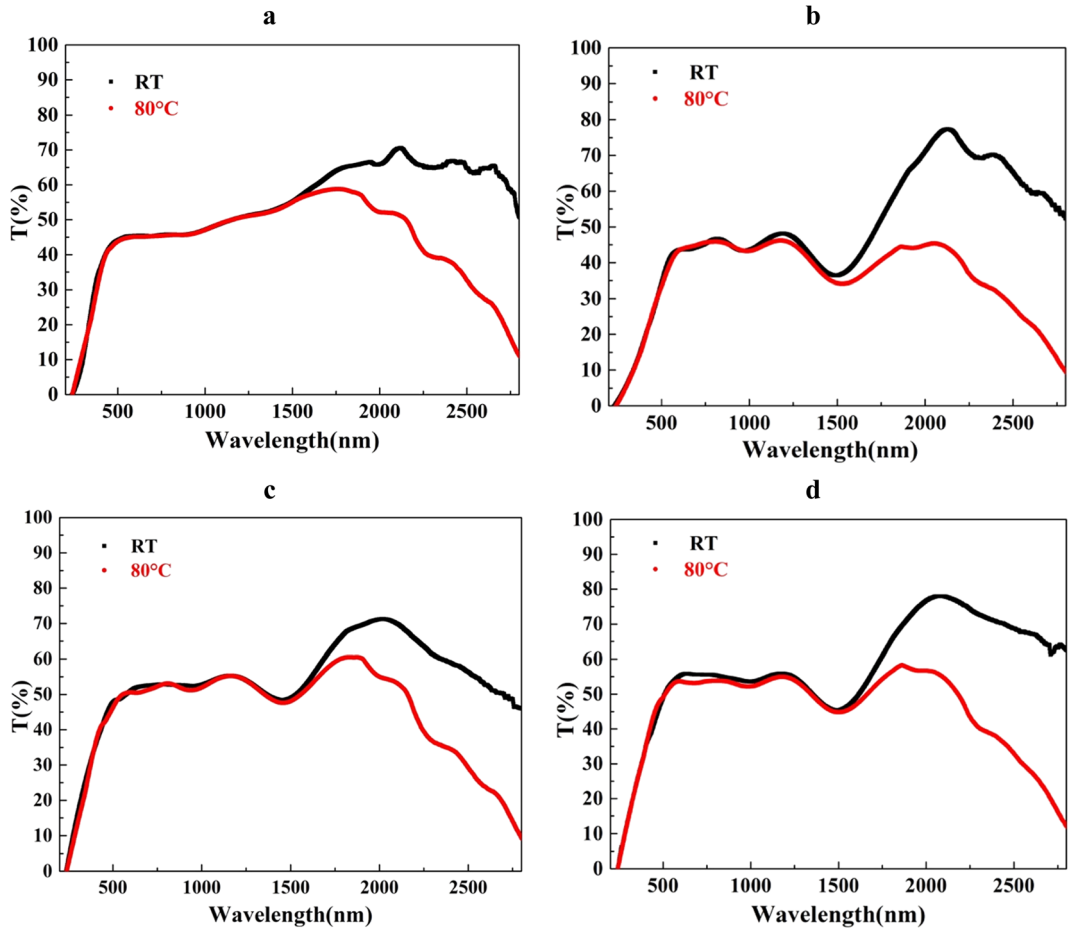

Fig. 6 Transmittance spectra at RT and 80 °C of (a) V, (b) W–V–W, (c) MoW–V–W, and (d) Mo–V–W samples.

$3.78 \times 10^2\ \Omega\ cm^{-2}$ and the lowest T_c of 36.8 °C. However, this sample presents the highest hysteresis ΔH of 14.8 °C.

A longstanding debate surrounds the nature of the metal–insulator transition (MIT) in VO_2. Some argue for a Mott-type transition, emphasizing strong electron–electron correlations, while others advocate for a Peierls-type transition, focusing on structural changes involving V dimerization. Recently, a hybrid perspective has emerged, proposing that the MIT in VO_2 might be best described as a Mott-Peierls phase transition, suggesting that electron–electron correlations and V^{4+} dimerization contribute significantly to this transition.[51–53] As evidenced by the XPS findings, the W–V–W configuration exhibits a lower V^{4+}/V^{5+} ratio compared to the Mo–V–W configuration. Consequently, the T_c of the Mo–V–W samples is lower than that of the W–V–W samples. Despite the low T_c of Mo–V–W, the Mo migration to the VO_2 lattice results in a broadening of the phase transition peak (bigger ΔH); this effect is likely due to the substitution of V in the VO_2 lattice by Mo through doping. Mo will replace the position of V in the doping process because the radius of Mo^{6+} is more significant than that of V^{4+}, which results in the deformation of its crystalline structure due to the size mismatch. This disparity in ionic radii between Mo^{6+} and V^{4+} leads to decreased activation energy required for MIT, resulting in a bigger ΔH and a phase transition sharpness.[49,54–56] The work done by Fan *et al.*[57] indicated that the high defect concentration would cause a hysteresis loop or disappearance of the shifting effect.

5. Optical properties

The optical transmittance of samples was measured in visible (vis) and near-infrared (NIR) regions under two different temperatures (room temperature (RT); 25 °C and 80 °C) of the V, W–V–W, MoW–V–W, and Mo–V–W samples. It is evident from the presented results in Fig. 6 that the transmittance in the visible region remains relatively constant for all the samples. The following formulas were used to calculate the integrated solar transmittance (T_{sol}, 300–2500 nm) and luminous transmittance (T_{lum}, 380–780 nm)[58]:

$$T_{sol/lum} = \int_{sol/lum}^{\phi}(\lambda)T(\lambda)d\lambda \int_{sol/lum}^{\phi}(\lambda)T(\lambda)d\lambda$$

$$\Delta T_{sol} = T_{sol}(25\ ^\circ C) - T_{sol}(80\ ^\circ C)$$

In this case, $\varphi_{lum}(\lambda)$ is the standard luminous efficiency function for the human photopic vision, $T(\lambda)$ indicates the film transmittance at a wavelength (λ), and $\varphi_{sol}(\lambda)$ is the solar irradiance spectrum for air mass 1.5, which corresponds to the sun standing 37° above the horizon and ΔT_{sol} is the solar modulation ability.

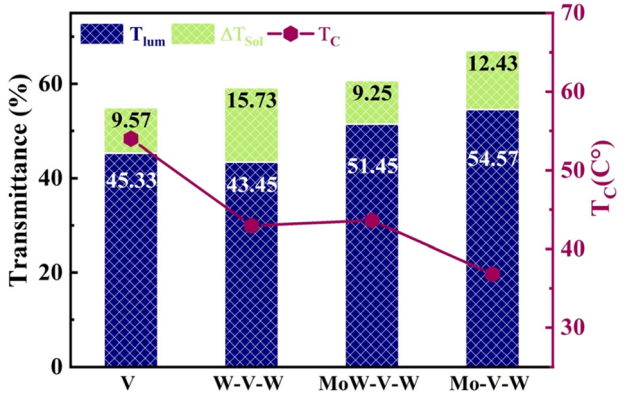

Fig. 7 Bar plots of T_{lum}, ΔT_{sol} and T_c of V, W–V–W, MoW–V–W and Mo–V–W samples.

To use VO_2 in smart windows applications, a technological obstacle is to raise the maximum T_{lum} to a respectable level (>50%) while preserving VO_2's high ΔT_{sol}.[59] The solar transmittance of each sample was computed as a means of illustrating the solar modulation. The calculated T_{sol} on the solar spectra present a similar comportment as T_{lum}. This suggests that the structures under investigation have a large impact on the transmission of not only in the visible light range but also in the entire solar spectra.

As presented in Fig. 7, T_{lum} calculated from the transmittance spectra at the RT, it presents a slight decrease from 45.33% to 41.65% in the W–V–W sample compared to the VO_2 thin films' reference sample (Table 3). The sandwich structure negatively affected the sample's transmittance in W–V–W due to the additional two WO_3 layers.[48] On the other hand, ΔT_{sol} increased to from 9.57% in VO_2 to 15.7%. Nevertheless, a considerable improvement in both MoW–V–W and Mo–V–W of 50.83% and 54.57% was noticed. In contrary to the W–V–W surface, the nanostructured surface of MoW–V–W and Mo–V–W acted as a light-harvesting media reducing the reflectance arrived from the VO_2 surface and acting as an antireflecting layer. Consequently, we notice a very promising improvement in T_{lum}. Additionally, in Table 3, T_{lum} improvement can be seen to have a direct relationship with the sandwich samples' optical band gap (E_g).[7,54] ΔT_{sol} decreases in Mo–V–W and MoW–V–W to 12.43% and 9.25%, respectively, compared to the W–V–W sample. It is believed that the defects generated due to the textured surface negatively affected the solar modulation of these two samples.

Table 3 T_c, T_{lum}, T_{sol} and ΔT_{sol} of V, W–V–W, MoW–V–W and Mo–V–W samples

Samples	T_{lum}	T_{sol}	ΔT_{sol}	T_c (°C)
V	45.33	46.86	9.57	54
W–V–W	41.65	43.45	15.73	43
MoW–V–W	50.83	51.45	9.25	43.6
Mo–V–W	54.57	52.49	12.43	36.8

IV. Conclusions

In conclusion, the systematic investigation of nanowire-based sandwich-structured thin films composed of $Mo_{0.2}W_{0.8}O_3$, MoO_3, and WO_3 top layers *via* physical vapor deposition provides a detailed understanding of their structural, electrical, and optical characteristics. Raman spectroscopy confirms the successful preparation of each thin film, highlighting distinctive vibrational modes and lattice features. FE-SEM images reveal a fascinating evolution of nanostructures, particularly with MoO_3 as the top layer, showcasing potential applications in smart window applications. Electrical properties exhibit significant improvements in conductivity for samples with MoO_3 as a window layer, attributing this enhancement to the migration of Mo atoms into the VO_2 lattice. The observed MIT behavior is rationalized based on XPS findings. Furthermore, optical analysis demonstrates promising improvements in luminous transmittance and solar modulation, especially in configurations with MoO_3 as the top layer. Collectively, these findings contribute to the knowledge base for developing and optimizing multifunctional thin films, paving the way for potential advancements in smart window technologies.

Data availability

Will be available on request.

Conflicts of interest

The authors declare that they have no known competing financial interests or personal relationships that could have appeared to influence the work reported in this paper.

Acknowledgements

The authors acknowledge the support from the Scientific Research Projects Coordination (BAP) – Konya Necmettin Erbakan University (NEÜ), under Project Number: 191319007 for Yasin Ramazan Eker and Mohamed A. Basyooni. The authors also acknowledge the support from the Science and Technology Research and Application Center (BITAM), Konya Necmettin Erbakan University (NEÜ).

References

1 P. Huovila, *et al.*, *Buildings and climate change: Summary for decision-makers*, 2009.
2 L. Pérez-Lombard, J. Ortiz and C. Pout, A review on buildings energy consumption information, *Energy Build.*, 2008, **40**(3), 394–398.
3 Z. Zhang, *et al.*, Thermochromic Energy Efficient Windows: Fundamentals, Recent Advances, and Perspectives, *Chem. Rev.*, 2023, **123**(11), 7025–7080.
4 K. Okimura, *et al.*, High luminous transmittance and solar modulation of VO_2-based smart windows with SiO_2 anti-

reflection coatings, *Sol. Energy Mater. Sol. Cells*, 2023, **251**, 112162.
5 M. K. Shahzad, *et al.*, Influence of VO_2 based structures and smart coatings on weather resistance for boosting the thermochromic properties of smart window applications, *RSC Adv.*, 2022, **12**(48), 30985–31003.
6 J. Victor, *et al.*, From multilayers to $V_{1-x}W_xO_2 \pm \delta$ films elaborated by magnetron sputtering for decreasing thermochromic transition temperature, *J. Alloys Compd.*, 2021, **858**, 157658.
7 D. Zhou, *et al.*, Symmetrical SnO_2/W-doped VO_2/SnO_2 sandwich structures with high luminous transmittance, excellent solar modulation ability and low phase transition temperature, *Infrared Phys. Technol.*, 2022, **123**, 104198.
8 H. Zhou, *et al.*, Surface plasmon resonance tunability in VO_2/Au/VO_2 thermochromic structure, *Laser Photonics Rev.*, 2014, **8**(4), 617–625.
9 Y. Dang, L. Zhao and J. Liu, Preparation and optical properties of W-doped VO_2/AZO bilayer composite film, *Ceram. Int.*, 2020, **46**(7), 9079–9085.
10 H. Zong, *et al.*, Preparation and characterization of HfO_2/VO_2/HfO_2 sandwich structures with low phase transition temperature, excellent thermochromic properties, and superior durability, *Ceram. Int.*, 2022, **48**(5), 6734–6744.
11 D. Malarde, *et al.*, Optimized atmospheric-pressure chemical vapor deposition thermochromic VO_2 thin films for intelligent window applications, *ACS Omega*, 2017, **2**(3), 1040–1046.
12 H. Koo, *et al.*, The effect of CeO2 antireflection layer on the optical properties of thermochromic VO_2 film for smart window system, *J. Mater. Eng. Perform.*, 2014, **23**, 402–407.
13 H.-T. Zhang, *et al.*, Wafer-scale growth of VO_2 thin films using a combinatorial approach, *Nat. Commun.*, 2015, **6**(1), 8475.
14 J. Kim, *et al.*, Two-dimensional VO_2 nanosheet converted from MXene for flexible thermochromic smart windows, *Chem. Eng. J.*, 2023, **477**, 147014.
15 H. Koo, *et al.*, Thermochromic properties of VO_2 thin film on SiNx buffered glass substrate, *Appl. Surf. Sci.*, 2013, **277**, 237–241.
16 G. Xu, *et al.*, Optimization of antireflection coating for VO_2-based energy efficient window, *Sol. Energy Mater. Sol. Cells*, 2004, **83**(1), 29–37.
17 H. Kim, *et al.*, Strain effect in epitaxial VO_2 thin films grown on sapphire substrates using SnO2 buffer layers, *AIP Adv.*, 2017, 7(10), 105116.
18 J. Zheng, S. Bao and P. Jin, TiO_2 (R)/VO_2 (M)/TiO_2 (A) multilayer film as smart window: Combination of energy-saving, antifogging and self-cleaning functions, *Nano Energy*, 2015, **11**, 136–145.
19 S. Long, *et al.*, Thermochromic multilayer films of WO_3/VO_2/WO_3 sandwich structure with enhanced luminous transmittance and durability, *RSC Adv.*, 2016, **6**(108), 106435–106442.
20 S.-Z. Sheng, *et al.*, Nanowire-based smart windows combining electro-and thermochromics for dynamic regulation of solar radiation, *Nat. Commun.*, 2023, **14**(1), 3231.
21 L. Veeramuthu, *et al.*, Novel stretchable thermochromic transparent heaters designed for smart window defroster applications by spray coating silver nanowire, *RSC Adv.*, 2019, **9**(61), 35786–35796.
22 L. L. Zhao, *et al.*, Enhanced Thermochromic Properties and Solar-Heat Shielding Ability of W_x V_{1-x} O_2 Thin Films with Ag Nanowires Capping Layers, *J. Nanosci. Nanotechnol.*, 2015, **15**(11), 9192–9196.
23 D. Y. Lu, *et al.*, Raman study of thermochromic phase transition in tungsten trioxide nanowires, *Appl. Phys. Lett.*, 2007, **90**(4), 041919.
24 W. Y. Wu, *et al.*, Thermochromism from Ultrathin Colloidal Sb2Se3 Nanowires Undergoing Reversible Growth and Dissolution in an Amine–Thiol Mixture, *Adv. Mater.*, 2019, **31**(4), 1806164.
25 K. C. Kam and A. K. Cheetham, Thermochromic VO_2 nanorods and other vanadium oxides nanostructures, *Mater. Res. Bull.*, 2006, **41**(5), 1015–1021.
26 M. A. Basyooni, *et al.*, Efficient $MoWO_3/VO_2/MoS_2$/Si UV Schottky photodetectors; MoS_2 optimization and monoclinic VO_2 surface modifications, *Sci. Rep.*, 2020, **10**(1), 1–18.
27 K. Appavoo, *et al.*, Role of defects in the phase transition of VO_2 nanoparticles probed by plasmon resonance spectroscopy, *Nano Lett.*, 2012, **12**(2), 780–786.
28 M. A. Basyooni, *et al.*, Fast response of CO2 room temperature gas sensor based on Mixed-Valence Phases in Molybdenum and Tungsten Oxide nanostructured thin films, *Ceram. Int.*, 2020, **46**(7), 9839–9853.
29 M. Currie, M. A. Mastro and V. D. Wheeler, Atomic layer deposition of vanadium dioxide and a temperature-dependent optical model, *J. Visualized Exp.*, 2018, (135), e57103.
30 A. Makarevich, *et al.*, Chemical synthesis of high quality epitaxial vanadium dioxide films with sharp electrical and optical switch properties, *J. Mater. Chem. C*, 2015, **3**(35), 9197–9205.
31 X.-B. Chen, Assignment of the Raman modes of VO_2 in the monoclinic insulating phase, *J. Korean Phys. Soc.*, 2011, **58**, 100–104.
32 T. Nagyné-Kovács, *et al.*, Hydrothermal synthesis and gas sensing of monoclinic MoO_3 nanosheets, *Nanomaterials*, 2020, **10**(5), 891.
33 P. Martín-Ramos, *et al.*, α-MoO_3 crystals with a multilayer stack structure obtained by annealing from a lamellar MoS_2/g-C_3N_4 nanohybrid, *Nanomaterials*, 2018, **8**(7), 559.
34 T. Ivanova, K. Gesheva and A. Szekeres, Structure and optical properties of CVD molybdenum oxide films for electrochromic application, *J. Solid State Electrochem.*, 2002, **7**, 21–24.
35 C. W. Kee, Assignment of O–O and Mo = O stretching frequencies of molybdenum/tungsten complexes revisited, *J. Chem.*, 2015, **2015**, 10.
36 A. Klinbumrung, T. Thongtem and S. Thongtem, Characterization of orthorhombic α-MoO_3 microplates produced by a microwave plasma process, *J. Nanomater.*, 2012, **2012**, 10.

37 F. Haque, *et al.*, Ordered intracrystalline pores in planar molybdenum oxide for enhanced alkaline hydrogen evolution, *J. Mater. Chem. A*, 2019, **7**(1), 257–268.
38 F. Liu, *et al.*, Ultrathin tungsten oxide nanowires: oleylamine assisted nonhydrolytic growth, oxygen vacancies and good photocatalytic properties, *RSC Adv.*, 2015, **5**(94), 77423–77428.
39 J. Díaz-Reyes, *et al.*, Characterization of WO_3 thin films grown on silicon by HFMOD, *Adv. Condens. Matter Phys.*, 2013, **2013**, 9.
40 H. Choi, *et al.*, Mid-infrared properties of a VO_2 film near the metal-insulator transition, *Phys. Rev. B: Condens. Matter Mater. Phys.*, 1996, **54**(7), 4621.
41 M. A. B. Mohamed, *VO_2 İnce Film İçeren İki Boyutlu ve Çok Katmanlı Yapılardaki Arayüzey Gerilmelerinin Termokromik ve Fotodetektör Performanslara Etkisi,* Necmettin Erbakan University, Turkey, 2020.
42 J. Díaz-Reyes, *et al.*, Characterization of WO3 thin films grown on silicon by HFMOD, *Adv. Condens. Matter Phys.*, 2013, **2013**, 9.
43 M. A. Basyooni, *et al.*, Tuning the metal–insulator transition properties of VO_2 thin films with the synergetic combination of oxygen vacancies, strain engineering, and tungsten doping, *Nanomaterials*, 2022, **12**(9), 1470.
44 S.-Y. Li, *et al.*, Thermochromic VO_2 nanorods made by sputter deposition: Growth conditions and optical modeling, *J. Appl. Phys.*, 2013, **114**(3), 033516.
45 T. D. Vu, *HiPIMS deposition of VO_2 thermochromic coating for enhanced optical properties, 2022.*
46 Z. Li, L. Gao and S. Zheng, SEM, XPS, and FTIR studies of MoO3 dispersion on mesoporous silicate MCM-41 by calcination, *Mater. Lett.*, 2003, **57**(29), 4605–4610.
47 V. Sreelakshmi, A. A. Kaliani and M. Jithin, Photochromic and hydrophilic vanadium oxide–molybdenum oxide composite thin films, *J. Mater. Sci.: Mater. Electron.*, 2023, **34**(3), 179.
48 Z. Fang, *et al.*, VO_2/ZnO bilayer films with enhanced thermochromic property and durability for smart windows, *Appl. Surf. Sci.*, 2021, **540**, 148414.
49 F. Chen, *et al.*, Simultaneous tuning of the phase transition temperature and infrared optical properties of Mo-doped VO_2 powders for intelligent infrared stealth materials, *Ceram. Int.*, 2023, **49**(15), 25585–25593.
50 D. Li, *et al.*, Influence of the charge compensation effect on the metal–insulator transition of Mg-W co-doped VO_2, *Appl. Surf. Sci.*, 2022, **579**, 151990.
51 N. F. Mott, The basis of the electron theory of metals, with special reference to the transition metals, *Proc. Phys. Soc., Sect. A*, 1949, **62**(7), 416.
52 C. Ling, *et al.*, W Doping and Voltage Driven Metal-Insulator Transition in VO Nano -Films for Smart Switching Devices, *ACS Appl. Nano Mater.*, 2019, **2**(10), 6738–6746.
53 S. Biermann, *et al.*, Dynamical singlets and correlation-assisted peierls transition in VO_2, *Phys. Rev. Lett.*, 2005, **94**(2), 026404.
54 C. Kang, *et al.*, Transformation of crystalline structure and photoelectric properties in VO_2/glass thin films by inserting TiO_2 buffer layers, *Appl. Surf. Sci.*, 2019, **463**, 704–712.
55 C. W. Jo, H. J. Kim and J. W. Yoo, Thermochromic Properties of W-Mo Co-Doped VO(M) Nanoparticles According to Reaction Parameters, *J. Nanosci. Nanotechnol.*, 2017, **17**(5), 2923–2928.
56 Y. Xue and S. Yin, Element doping: a marvelous strategy for pioneering the smart applications of VO_2, *Nanoscale*, 2022, **14**(31), 11054–11097.
57 L. Fan, *et al.*, Modulation of VO_2 metal-insulator transition by co-doping of hydrogen and oxygen vacancy, *Sol. Energy Mater. Sol. Cells*, 2020, **212**, 110562.
58 M. A. Abozeid, *et al.*, Development of nano-WO_3 doped with NiO for wireless gas sensors, *Arabian J. Sci. Eng.*, 2019, **44**(1), 647–654.
59 M. Zhou, *et al.*, Periodic porous thermochromic VO_2 (M) films with enhanced visible transmittance, *Chem. Commun.*, 2013, **49**(54), 6021–6023.